Research Square

Preprints are preliminary reports that have not undergone peer review.
They should not be considered conclusive, used to inform clinical practice,
or referenced by the media as validated information.

Acid–base speciation and nitro-group retention govern optical persistence during $\cdot$OH aging of nitrophenol brown carbon

Yanru Huo

huoyanru8@gmail.com

McGill University

Qingcheng Lan

McGill University

Alexander Logozzo

McGill University

Thomas Preston

McGill University

Article

Keywords:

Posted Date: November 24th, 2026

DOI: https://doi.org/10.21203/rs.3.rs-11773944/v1

License: This work is licensed under a Creative Commons Attribution 4.0 International License.
Read Full License

Additional Declarations: No competing interests reported.

Acid–base speciation and nitro-group retention govern optical persistence during ·OH aging of nitrophenol brown carbon

Yanru Huo[1*], Qingcheng Lan[1], Alexander Logozzo[2], Thomas C. Preston[1,2*]

[1]Department of Atmospheric and Oceanic Sciences, McGill University, Montreal, Quebec, Canada.
[2]Department of Chemistry, McGill University, Montreal, Quebec, Canada.

*Corresponding authors: huoyanru8@gmail.com; thomas.preston@mcgill.ca

Abstract

Brown carbon warms the atmosphere and can keep absorbing sunlight while oxidation consumes its molecules, but what controls this persistence remains unclear. Here, electronic-structure and kinetic calculations for six aqueous nitrophenols show that phenolic deprotonation leaves hydroxyl-radical reactivity near the diffusion limit but red-shifts and strengthens visible absorption. Titrations and UV–visible measurements reproduce this spectral transition. Reaction-pathway calculations show that early oxidation adds hydroxyl groups while retaining the nitroaromatic chromophore; only higher-barrier denitration and ring opening bleach it. A kinetic–optical model built from these barriers and spectra predicts that absorption decays two to three times more slowly than 4-nitrophenol, as measured at pH 2. Molecular-polarizability and radiative-transfer calculations show that, through the complex refractive index, deprotonation increases the atmospheric shortwave forcing of 4-nitrophenol and its nitroaromatic products up to 2.4-fold. Acid–base speciation thus sets how strongly nitrophenol brown carbon absorbs, and nitro-group retention how long that absorption survives oxidative processing.

Keywords: brown carbon | aerosol pH | aqueous aging | complex refractive index | radiative forcing

Introduction

Climate change has driven an increase in the frequency and intensity of wildfires globally, resulting in unprecedented burned areas in several countries [1–3]. These large-scale fires emit significant amounts of carbonaceous aerosols, primarily in the form of black carbon (BC) and organic carbon (OC) [4]. Within the OC fraction, a subset known as brown carbon (BrC) exhibits light-absorbing properties [4]. BrC aerosols are ubiquitous in the troposphere and can effectively absorb tropospheric solar radiation at near-ultraviolet (NUV) and visible (vis) wavelengths

[5–7]. On a global scale, the direct radiative effect of BrC (+0.10 W m^{-2}) is more than 25% of the radiative forcing from black carbon (BC, +0.39 W m^{-2}) [6]. Unlike black carbon, BrC undergoes atmospheric photochemical processing that can substantially alter its light-absorbing properties, including through photobleaching [8, 9]. Photobleaching leads to significant changes in the absorptive properties of BrC aerosols and thereby alters atmospheric radiative forcing [10]. Witkowski et al. observed that ·OH bleaches 4-nitrophenol solutions at both pH 2 and pH 9 but that the bleaching lags the loss of the parent compound by factors of 3 and 1.5, respectively, because light-absorbing by-products are formed [11]. Thus, it is imperative to investigate how reaction mechanisms control the optical properties and radiative effects of BrC during aging.

Nitrophenols are widely detected atmospheric BrC chromophores and can contribute appreciably to near-UV and visible light absorption [12–15]. They occur in both the gas and condensed phases, including atmospheric particles and cloud, fog, and rainwater [16]. In atmospheric aqueous phases, oxidation by hydroxyl radicals (·OH) contributes to the daytime transformation of nitrophenols and can alter both their chemical composition and light absorption [11, 17]. Because atmospheric particles and cloud droplets span a broad range of acidity [18], acid–base speciation can substantially modify the optical properties of BrC [19, 20]. The visible absorption spectra of nitrophenols are strongly pH dependent [21, 22]. pH can therefore modulate the evolution of light absorption during aqueous-phase ·OH aging, with implications for the radiative effects of BrC [11, 19, 20].

The complex refractive index (RI), $m = n + ik$, plays a key role in determining the optical characteristics and climate relevance of BrC aerosols [23]. The real part (n) primarily governs refraction and scattering, whereas the imaginary part (k) describes absorption. Changes in chemical composition and molecular polarizability therefore translate into changes in aerosol optical properties and radiative effects [24–26]. However, such optical characterization does not resolve how acid–base speciation couples molecular reactivity to optical persistence in nitrophenol BrC. A ·OH-initiated reaction mechanism has been proposed from aqueous photoreactor experiments [11], but the energetics and kinetic competition among individual elementary steps, and how they control the evolving absorption, remain poorly constrained. Recent computational studies have shown that explicit exploration of atmospheric reaction networks can reveal previously unresolved branching pathways and key mechanistic branch points [27]. More broadly, oxidative processing can lead to substantial bleaching or to persistent light absorption, depending on the chromophore and oxidation conditions [7, 11].

Here, we systematically investigated the effect of pH on the aging mechanisms and optical properties of BrC during ·OH oxidation. We combined measured and calculated UV–visible (UV–Vis) spectra with computed reaction kinetics, complex RI, and shortwave forcing calculations to assess how deprotonation changes BrC aging in aqueous atmospheric media. This study provides a mechanistic framework for evaluating whether nitrophenols, an important class of strongly light-absorbing BrC chromophores, can retain or enhance visible-light absorption during daytime processing.

Results

Speciation and ·OH reactivity

The pH of the atmospheric aqueous phase selects, through the pK_a of each chromophore, the species that reacts, and with it the aging mechanism and its optical outcome [28]. We computed the ·OH-initiated reactions of the six nitrophenols in their neutral and phenol-deprotonated forms, with $\Delta G^{\ddagger}$ and $\Delta_r G$ from DFT and rate constants from transition state theory (Methods). The channels comprise radical adduct formation (RAF), hydrogen atom abstraction from a ring carbon (HAAben) or from a substituent (HAAsub), and single-electron transfer (SET) (Supplementary Fig. 1), with the free-energy surfaces in Supplementary Figs. 2–7 and the distributions of $\Delta G^{\ddagger}$ and $\Delta_r G$ in Supplementary Figs. 8 and 9. $\Delta G^{\ddagger}$ increases with the electron-withdrawing strength of the ring substituents, as expected for the electrophilic ·OH, which in hydrogen abstraction acts as a neutral radical with an electrophilic-like preference for electron-rich C–H bonds. For the neutral species the lowest barriers are the RAF routes ($\Delta G^{\ddagger}$ = 5.33–11.38 kcal mol^{-1}), in line with hydroxyl addition to the ring being the common first oxidation step [29–31], and the HAA and SET channels lie at 8.33–47.77 kcal mol^{-1} (Supplementary Figs. 2–4 and 8). For the phenol-deprotonated species the SET barriers fall to 0.01–0.39 kcal mol^{-1} (Supplementary Fig. 8h), as found for deprotonated parabens in water [32], because the electron-rich anion gives up an electron more readily, although each anion also has RAF or HAA channels with barriers of 2.45 kcal mol^{-1} or less (Supplementary Figs. 5–7). Nearly all RAF and HAA steps are exergonic, whereas SET is endergonic for the neutral species ($\Delta_r G$ = 14.69–32.62 kcal mol^{-1}) and exergonic for the phenol-deprotonated species (−12.67 to −2.31 kcal mol^{-1}) (Supplementary Figs. 2–7 and 9).

Rate constants were obtained by summing the transition-state-theory rate constants of all channels of a compound, with the bimolecular channels referred to the 1 M standard state and

corrected for the solvent cage, and applying the Collins–Kimball diffusion correction to the sum, so that no total exceeds the Smoluchowski rate constant k_D of the encounter pair, 7.8–8.1 $\times 10^9$ M^{-1} s^{-1} at 298 K (Supplementary Note 2 and Supplementary Table 6). The computed totals of the neutral species at 298 K range from 1.1×10^8 M^{-1} s^{-1} for 5NSA to 8.1×10^9 M^{-1} s^{-1} for 4NS, with 4NP, 4NC, 4NGA and 4M5NC at 0.56, 0.71, 0.88 and 0.99 k_D, and they rise with temperature and fall with viscosity (Fig. 1c,d and Supplementary Tables 7 and 8), whereas the phenol-deprotonated species have summed chemical rate constants 2.6×10^4 to 2.1×10^8 times k_D at 298 K and lie at the diffusion limit at every temperature, and $5NSA^-$, whose carboxylate is deprotonated while its phenolic hydroxyl is not, is computed at 8.1×10^9 M^{-1} s^{-1} (Supplementary Table 8). Among the neutral species log k increases with E_{HOMO} ($R^2 = 0.72$; Fig. 1a), as expected for an electrophilic radical, with the range compressed as the more reactive compounds approach k_D, and deprotonation of the phenol brings every compound to k_D, raising k by factors of 1.8 and 1.4 for 4NP and 4NC and changing it by less than 15% for 4M5NC, 4NS and 4NGA, which already react close to the diffusion limit (Fig. 1b).

Measurements exist for the parent compound and test the absolute scale: the three literature values for 4NP at pH < 3 compiled by Witkowski et al. lie between 3.8 and 6.2×10^9 M^{-1} s^{-1} [11, 33, 34], pulse radiolysis gives 4.1×10^9 M^{-1} s^{-1} at pH 5.2 and twice that value at pH 9.2 [34], and the anion is assigned 8.7×10^9 M^{-1} s^{-1} [11, 34]. The calculations reproduce both forms, 4.4×10^9 M^{-1} s^{-1} for neutral 4NP and 7.9×10^9 M^{-1} s^{-1} for the anion, and the factor of 1.8 between them (Supplementary Note 2), so the loss rate of the phenols changes by a factor of two at most across the phenolic pK_a, far less than the visible absorption. At the less acidic end of the atmospheric range, which reaches pH 8 in cloud water [20], both forms of 4NP react near the diffusion limit, as found for phenols + ·OH [17], and the rate constant measured for 4NC at pH 7, (3.14–4.81) $\times 10^{10}$ M^{-1} s^{-1} [17], lies above the Smoluchowski limit used here, which rests on Stokes–Einstein diffusion coefficients and therefore underestimates the mobility of a species as small as ·OH. What deprotonation of the phenol changes is the mixture of channels: below pK_{a1}, RAF dominates for all six compounds, with HAA contributing 18% for 4NGA, whereas for the phenol-deprotonated species, which react at the diffusion limit, RAF carries most of the flux for $4NP^-$, $4M5NC^-$, $4NS^-$ and $4NGA^-$, HAA becomes competitive for $4NC^-$, and SET carries less than 2% despite its sub-kcal barriers (Supplementary Fig. 10). The computed pH dependence of k is compared with the measured values in Fig. 1e.

Aging pathways of 4NP

4NP, the simplest nitrophenol BrC, was selected as a proxy to study the subsequent aqueous-phase aging mechanisms initiated by ·OH. As summarized in Fig. 2, the proposed chemistry can be grouped into four stages: (i) formation of the early aromatic products P1 and 4NC (P2), with 4NC acting as a key intermediate; (ii) secondary hydroxylation of 4NC while retaining the aromatic chromophore; (iii) conversion to quinone-like and denitrated polyhydroxy aromatics (P3, P7, and P8); and (iv) deep oxidation/ring opening to P4 and P9. In this scheme 4NC is the central intermediate from which the later branches emerge.

The early stage starts with single-electron transfer from $4NP^-$ to ·OH, which forms the 4-nitrophenoxyl radical (IM1) over a barrier of 0.39 kcal mol^{-1}. Although this channel carries a minor share of the initial flux, most of which goes to ·OH addition at the nitro-substituted carbon (2.45 kcal mol^{-1}; Supplementary Figs. 5 and 10), the 4NC yield of 0.40 measured at pH 9 [11] shows that this adduct does not, for the most part, lose its nitro group, and the SET route is followed here because it leads to 4NC, the product detected experimentally (Supplementary Note 5). Addition of ·OH to the carbon-centered resonance form of IM1 (IM2) yields 6-hydroxy-4-nitrocyclohexa-2,4-dien-1-one (IM3) with a barrier of 15.92 kcal mol^{-1}. In the aqueous phase, abstraction of an H atom or H^+ from IM3 yields 2-hydroxy-4-nitrocyclohexa-2,5-dien-1-one (P1) and the active anionic intermediate IM4, with free-energy barriers of 7.12 and 15.29 kcal mol^{-1}, respectively. Although the barrier to P1 is the lower of the two, the two steps consume different co-reactants: ·OH, present at roughly 10^{-15} M in the aqueous phase, and water at 55.5 M. On a pseudo-first-order basis the route to 4NC is therefore favored by about eleven orders of magnitude (Supplementary Note 5), consistent with 4NC rather than P1 being the product detected experimentally. Transfer of H atoms from water to IM4 then forms 4NC (P2) and is feasible ($\Delta G^{\ddagger}$ = 10.07 kcal mol^{-1}). An alternative route begins with ortho addition of ·OH to 4NP, followed by O_2 addition and HO_2· elimination to yield 4NC ($\Delta G^{\ddagger}$ = 25.31 kcal mol^{-1}); disproportionation of the resulting o-DHNCD radical can also produce 4NC. Witkowski et al. [11] detected 4NC experimentally under acidic conditions (pH = 2), supporting the importance of this early aromatic stage.

Once formed, 4NC undergoes additional aromatic functionalization. Electrophilic addition of ·OH at the carbon adjacent to the $–NO_2$ group forms IM6, and subsequent O_2 addition and HO_2· elimination yield the quinone-like intermediate IM8. P1 can also feed into IM8

through ·OH addition. IM8 then undergoes denitration and proton-transfer steps to form hydroxy-1,4-benzoquinone (P3), consistent with previous detection of quinone products in aqueous hydroxylation experiments [35, 36]. Parallel ·OH addition to alternative aromatic carbon sites on 4NC yields the positional isomers 5-nitropyrogallol (P5) and 4-nitropyrogallol (P6), both of which have been detected experimentally [11]. Another branch from IM6 proceeds through a pre-reaction complex and NO_2^- loss to generate the radical precursor to benzene-1,2,4-triol (P7); the resulting IM23 radical then forms P7 together with P3 via intermolecular disproportionation. In a related pathway, para addition of ·OH to 4NP forms IM24, which after O_2 addition and HO_2· elimination yields benzoquinone (P8) with barriers of 9.58–18.21 kcal mol^{-1}. These reactions define the later aromatic-oxidation stage of Fig. 2, in which the ring is retained but the chromophore becomes more strongly functionalized.

Deep oxidation to small ring-opening products appears to be much less favorable for ·OH alone. Although P3 can, in principle, undergo further reactions to produce glyoxylic acid (P9), the decisive H-transfer step requires a barrier of 41.53 kcal mol^{-1}. Likewise, conversion of the o-peroxy radical to nitroglyoxal (P4) is hindered by a high barrier of 31.78 kcal mol^{-1}, and formation of the required o-peroxy radical is itself kinetically disfavored because of spin constraints, resonance stabilization of the aromatic radical, and steric hindrance. The direct pathway from IM24 through NO_2^- elimination (IM27) and proton loss to IM28 is also not feasible, because the proton-loss step has a barrier of 83.29 kcal mol^{-1}. Taken together, these results indicate that ·OH aging predominantly forms more strongly absorbing aromatic products, whereas ring opening by ·OH alone is slow relative to functionalization and is accelerated by subsequent oxidation by species such as ozone once polyhydroxy aromatic compounds have formed [37].

To test whether this pathway ordering is quantitatively consistent with observation, we assembled the computed barriers, rate constants and TD-DFT spectra into a lumped kinetic–optical box model in ·OH-exposure coordinates (Supplementary Note 5). With a single fragmentation branching parameter constrained by the measured non-aromatic carbon fraction, the model predicts that the absorbance integrated over 250–600 nm decays 2.5–3.1 times more slowly than 4NP at pH 2 and 2.5–2.9 times more slowly at pH 9, and it gives a peak 4NC yield of 0.22–0.25 at pH 2, close to the measured 0.20, without adjustment. Propagating the uncertainties of the computed barriers, rate constants, spectra and product pK_a values in 3000 Monte Carlo draws gives $R > 1.5$ at pH 2 in 99% of draws (Supplementary Note 5). The measured lags are 3.0 at pH 2 and 1.5 at pH 9 [11], so the model captures the magnitude of the lag, which follows from

the barrier ordering alone, but not its decrease with pH. Adjusting the ·OH chemistry does not close this gap: across the Monte Carlo draws, and for a pH-dependent fragmentation branching or denitration of the anionic adduct, a lower R at pH 9 comes with a lower peak 4NC yield, which is already below the measured 0.40 (Supplementary Note 5). The gap more likely reflects a process the model omits. Direct photolysis is one candidate: the deprotonated nitropyrogallols absorb about three times more strongly at the 254 nm photolysis wavelength than their neutral forms, so photolysis, which the model built for the ambient aqueous phase does not include, would bleach the pH 9 mixture faster.

Speciation and absorption spectra

After ·OH aging the molecular structure of BrC changes substantially [38], and the UV–Vis spectra of the deprotonated species are red-shifted relative to the neutral species (Fig. 3a–f). This trend has also been observed in fulvic acid, water-soluble carbon [39], and humic substances [40, 41]: as pH increases, the absorption spectra typically shift to longer wavelengths and exhibit stronger absorption. The greater the electron-donating capacity of the side-chain groups, the greater the red shift of the UV–Vis spectrum. Deprotonated species also exhibit substantially stronger visible-region absorption than neutral species, implying that neutral to weakly alkaline BrC aerosols can absorb more solar radiation than more acidic particles. This behavior is consistent with field observations that BrC can be highly sensitive to pH changes [20, 42]. To validate the reliability of the calculated results, we measured UV–visible spectra of selected BrC molecules. For the neutral species, the calculated absorption maxima reproduce the experimental values within 15 nm. For $4NC^{-}$, the calculations capture the ordering and general spectral region of the main absorption bands. Accordingly, the calculations capture peak positions, band ordering, and relative intensities within the expected uncertainty for these BrC molecules. The pH-dependent changes in nitrophenols' absorption peaks arise from dissociation of their phenolic hydroxyl groups. In Fig. 3g–k, with increasing pH values, UV–Vis spectra show an initial absorption peak at ~310–350 nm when pH < pK_{a1}; once pH > pK_{a1}, the peak red-shifts and a stronger band emerges at 400–440 nm. In Fig. 3l, 5NSA predominantly exists as the singly deprotonated carboxylate form ($COOH \rightarrow COO^{-}$) over $2.37 < pH < 9.68$. As this group is only weakly conjugated with the nitrophenol chromophore, the UV–Vis bands show little shift. The phenolic O–H that would strongly affect the chromophore deprotonates only at pH > pK_{a2} (9.68), with internal H-bonding further damping any changes.

The calculated absorption properties of transformation products in the aqueous phase are presented in Fig. 4 and Supplementary Fig. 11. The transformation products can be divided into three types: quinones (P1, P3, and P8); hydroxyl adducts (P2, P5, P6, and P7); and ring-opening products (P4 and P9). Among the quinones, increasing functionalization produces a red shift, with absorption moving from P8 (172 and 258 nm) to P3 (184 and 267 nm) to P1 (267 and 429 nm). The UV–Vis spectra likewise show that increasing hydroxyl substitution leads to a red shift due to enhanced conjugation (P2, P5, P6, and P7). This also explains the experimentally observed red shift of BrC droplets during aging [43]. Introduction of nitro groups further extends absorption into longer wavelengths, attributed to additional n$\rightarrow \pi^*$ transitions and intramolecular charge-transfer effects. The maximum absorption peaks of ring-opening products (P4 and P9) are more likely to occur in the vacuum ultraviolet (VUV) region than for aromatic compounds. P9 shows an intense ($\pi \rightarrow \pi^*$) band near 160 nm and a weaker (n$\rightarrow \pi^*$) feature around 215 nm, whereas carbonyl–nitro orbital mixing in P4 lowers the excitation energy and shifts the dominant absorption to approximately 180 nm. These calculations therefore support a picture in which ·OH oxidation initially generates functionalized aromatic products that retain strong visible absorption, whereas extensive ring opening would shift absorption out of the near-UV/visible and weaken the BrC chromophore.

Complex refractive index

Figure 4a–d and Supplementary Figs. 12–14 show the accurate fitting (R^2= 0.9496–0.9981) of the imaginary part of the molecular polarizability, Im[$\alpha(\lambda)$]. Based on this, curves of the real and imaginary part of complex RI as a function of wavelength were obtained, shown in Fig. 4e–l and Supplementary Figs. 15–18. The refractive index is that of the particle phase at 85% relative humidity, with the solute number density c_s taken from the molecular dynamics simulations that also supply the particle densities (Supplementary Note 3 and Supplementary Table 5), and since k scales with c_s at these concentrations, the absolute values of k and of the forcing below refer to this composition. The calculated $n(\lambda)$ and $k(\lambda)$ for 4NC are consistent with the result reported by Knight et al. [22] from a physically based mixing rule. For neutral species of BrC, the n values show clear wavelength-dependent dispersion from 200 nm to 400 nm for all species (Fig. 4e). Most compounds follow a broadly similar trend, with a weak maximum at shorter wavelengths near 210 nm, a shallow minimum near ultraviolet radiation B (UVB, 280–315 nm), and recovery toward longer wavelengths. 4NP exhibits substantially stronger light scattering, marked by a

pronounced decrease followed by a sharp rise above 320 nm, indicating a distinct optical response in the UVA region. For deprotonated species of BrC, the refractive-index dispersion is displaced toward longer wavelengths (Fig. 4f). Compared with the neutral and deprotonated forms of 4NP, the neutral ·OH-aging products (P1–P9), in Fig. 4g,h and Supplementary Fig. 15, exhibit weaker dispersion in the real part of the complex RI over the range of 200–500 nm. P4 and P9 show the weakest wavelength dependence, with nearly constant n values, whereas P3 and P8 display much stronger variation, including pronounced minima (257 nm and 249 nm) and sharp increases (286 nm and 278 nm). The products exist in either deprotonated or protonated forms over a wide pH range. In Supplementary Fig. 16, compared with neutral products, ionic products show stronger dispersion in n values, with broader variations and more obvious increases in the long-wavelength region. Ionization reshapes both the magnitude of n and its spectral dispersion in a strongly structure-dependent manner.

The imaginary part (k) of the complex RI for neutral BrC shows strong wavelength dependence due to molecular absorption (Fig. 4i) [25, 44]. The profiles are nonmonotonic, displaying an initial response near 204 nm, a relative minimum near 220–240 nm, and a broader increase again toward the UVA region before decreasing slightly over 350 nm. For deprotonated species of BrC, the peak of k is displaced toward longer wavelengths (Fig. 4j). Except for 5NSA, the deprotonated species absorb more strongly than their neutral counterparts. This result is consistent with previous observations that BrC absorption increases with increasing pH [19, 20, 45, 46]. Electron delocalization is enhanced, reducing the transition energy and resulting in stronger light absorption and a red shift. This explains why the brown coloration is observed in nitrophenols [47]. Notably, the k values of 4NP and $4NP^-$ exhibit the largest fluctuation amplitude, which arises from stronger and more localized electronic transitions within the UVA region. The light-absorption capacity of neutral products in the UVA region is significantly lower than that of the reactants (Fig. 4k,l and Supplementary Fig. 17). For example, quinone products (P3 and P8) and open-ring products (P4 and P9) exhibit virtually no light absorption in the UVA region. However, as the number of $-OH$ and $-NO_2$ on the benzene ring increases, light absorption gradually increases. Multiple hydroxyl groups typically enhance absorption intensity and promote red shift through enhanced resonance electron donation and electron delocalization. The $-NO_2$ group is a strong electron-withdrawing substituent that can enhance absorption at longer wavelengths. This effect is more pronounced in ionic products due to their strong electron-donating ability (Supplementary Fig. 18). Thus, light absorption in ionic products is enhanced and accompanied

by a significant red shift. This also explains why, among water-soluble organic carbon (WSOC) species, CHON species have the highest relative absorbance even though they are not the most abundant group [48].

Shortwave radiative forcing

Figure 5 shows how these optical differences translate into global-mean all-sky shortwave forcing for fresh (0–2 km) and lofted (2–5 km) smoke at low and high pH. Every species heats the atmosphere and dims the surface, consistent with absorption of solar radiation within the aerosol layer, and the atmospheric heating follows the aging sequence of Fig. 2: for fresh smoke at low pH, 4NP and the products that retain the nitro group (P1, 4NC, P5 and P6) heat the atmosphere by 0.8–1.2 W m^{-2} Tg^{-1}, the denitrated products P3, P7 and P8 by 0.3–0.9 W m^{-2} Tg^{-1}, and the ring-opening products P4 and P9 by less than 0.05 W m^{-2} Tg^{-1}, so that the forcing of P4 and P9 is almost entirely a top-of-atmosphere cooling by scattering. Deprotonation increases the atmospheric and surface forcing of 4NP, 4NC and P5 by a factor of 1.7–2.4 and that of P6 by a smaller margin, reflecting the red-shifted and intensified visible absorption of these species, whereas the deprotonated forms of P1, P3 and P7 force less than their neutral counterparts. Lofting the layer from 0–2 km to 2–5 km leaves the clear-sky forcing almost unchanged but increases the all-sky atmospheric heating of the aromatic species by 50–70%, because the cloud of the cloudy column shields a layer below it and returns reflected sunlight through a layer above it, and the same geometry sets the sign of the top-of-atmosphere forcing. The fresh layer, which lies below the cloud top, cools at the top of the atmosphere for every low-pH species and for all high-pH species except $4NC^-$ and $P5^-$, whose forcing is close to zero, whereas the lofted layer warms at the top of the atmosphere for every species whose atmospheric heating exceeds about 1 W m^{-2} Tg^{-1}, by up to 0.7 W m^{-2} Tg^{-1} at low pH and 1.7 W m^{-2} Tg^{-1} at high pH, as expected for absorbing aerosol above a bright cloud [49].

Discussion

This work provides molecular-level evidence that pH governs the optical properties of nitrophenol BrC during daytime aging and, through the reaction mechanism, the products that aging forms. Once pH exceeds the pK_a of the phenolic hydroxyl group, the deprotonated species absorb more strongly in the visible (400–440 nm) and react with ·OH at the diffusion limit, while the loss rate itself changes little: the measured rate constants of 4NP, 3.8–6.2 × 10^9 M^{-1} s^{-1} for

the neutral compound and 8.7×10^9 M^{-1} s^{-1} for the anion, both lie within about a factor of two of the diffusion limit, and the calculations, once the solvent-cage correction is included, reproduce both values. 5NSA, whose phenolic hydroxyl stays protonated below pH 9.68, is the exception, with spectra that change little over the atmospheric pH range. Loss of the parent does not, however, imply equally fast bleaching: the ensuing chemistry preferentially forms polyhydroxylated nitroaromatics that retain or enhance visible absorption, whereas the steps that destroy the chromophore (denitration and ring opening) carry higher barriers. A kinetic–optical model assembled from the computed barriers and spectra places the resulting lag at a factor of two to three in ·OH exposure, the magnitude measured at pH 2, while the smaller lag measured at pH 9 points to a process outside the ·OH chemistry, such as photolysis in the experiments, which the model does not include.

Taken together, these results indicate that aqueous ·OH processing of nitrophenol BrC need not lead to immediate bleaching. Where aromatic functionalization outcompetes denitration, aging can sustain or strengthen visible absorption and the associated atmospheric shortwave heating, so that early and intermediate aromatic products remain more climatically relevant than the deep-oxidation products [7]. The forcings reported here are idealized single-component, fixed-size, mass-normalized efficiencies, and the largest step toward ambient relevance is the chemistry these calculations deliberately exclude: because fragmentation by ·OH alone is slow relative to functionalization, the persistence of BrC absorption will depend on competition between aromatic functionalization and subsequent oxidation by species such as O_3, together with the effects of aerosol mixing state, size evolution, and cloud processing. Resolving that competition is an important requirement for incorporating pH-dependent BrC chemistry into atmospheric radiative-transfer and chemical-transport models [50].

Methods

Target chemicals and materials

Six atmospherically relevant nitrophenols were selected based on their detection in ambient atmospheric waters [51]. All chemicals were obtained from commercial suppliers and used without further purification: 4-nitrophenol (4NP, ≥99%), 4-nitrocatechol (4NC, 97%), and 4-nitroguaiacol (4NGA, 97%) from MilliporeSigma Canada Ltd.; 4-nitrosyringol (4NS, 98%) from

Fisher Scientific; 5-nitrosalicylic acid (5NSA, 99%) from MilliporeSigma Canada Ltd.; and 4-methyl-5-nitrocatechol (4M5NC, >95%) from Toronto Research Chemicals (LGC Standards).

The optimized structures and molar fractions based on the pK_a values of six selected nitrophenols are shown in Supplementary Fig. 19. The pK_a values of the target compounds were predicted using Chemicalize (ChemAxon) [52]. We experimentally determined the pK_a values of the target compounds (Supplementary Table 1; titration methods for pK_a in Supplementary Note 1), which deviated from the predicted values by less than 0.1 units for the phenolic hydroxyl groups, except for 4NGA (Supplementary Table 1). The largest deviations are observed for 5NSA and 4NGA, with differences of 0.48 and 0.94 (pK_a) units from the experimental values, respectively; note that the 5NSA deviation refers to its carboxylic acid pK_{a1} rather than a phenolic hydroxyl group. These deviations remain within an acceptable range for the qualitative use of the predicted (pK_a) values in the subsequent speciation analysis. The predicted values were deliberately used consistently across all compounds to avoid mixing pK_a values obtained using different conditions. The fraction of nitrophenol BrC existing as a doubly deprotonated species in the atmosphere is anticipated to be negligible, as its pK_a significantly exceeds the pH range commonly encountered in atmospheric aerosols and cloud droplets [22].

Mechanism computation

In this study, all electronic structure calculations were performed using the Gaussian 16 software package [53]. The geometry optimization and frequency calculation of all the reactants (R), transition states (TS), intermediates (IM), and products (P) were performed at the M06-2X/6-31+G(d,p) level. To obtain reliable calculated results, CCSD(T)/aug-cc-pVTZ, CBS-QB3, B3LYP/6-311+G(d,p), MP2/6-311+G(d,p), and M06-2X/6-311++G(3df,2p) were used to calculate the dissociation energy for phenolic hydroxyl groups of 4NP. An implicit solvation model was used to simulate the aqueous-phase environment [54, 55]. In Supplementary Table 2, the dissociation energy at M06-2X/6-311++G(3df,2p)/SMD is closest to that at CCSD(T)/aug-cc-pVTZ/SMD. Thus, M06-2X/6-311++G(3df,2p) was selected to calculate the single-point energy. The intrinsic reaction coordinate (IRC) calculations were performed to validate the authenticity of the transition states (TS). The Gibbs free energy of reaction ($\Delta_r G$) corresponds to the energy difference between P and R, while the activation free energy ($\Delta G^{\ddagger}$) refers to that between the TS and R. All free energies refer to the 1 atm standard state of the frequency calculations; the

conversion of the bimolecular rate constants to the 1 M standard state is made in the kinetic calculations (Supplementary Note 2).

Kinetic calculations

Rate constants for each elementary channel were computed with conventional transition-state theory. For the RAF and HAA channels, whose transition states were located, Wigner tunneling and reaction-path degeneracy were included, the rate constants were converted from the 1 atm to the 1 M standard state with the factor RT/p° (24.46 L mol^{-1} at 298 K), and the free-volume correction of Okuno for the solvent cage, $RT\{\ln[n\,10^{(2n-2)}] - (n-1)\}$ = 2.55 kcal mol^{-1} for $n = 2$ at 298 K [56, 57], was subtracted from the barriers. The barriers of the SET channels were obtained from Marcus theory, with the reorganization energy from the four-point scheme (Supplementary Note 2). The channel rate constants of each compound were summed and the sum was corrected for diffusion with the Collins–Kimball relation, $k = k_{\mathrm{chem}}k_{\mathrm{D}}/(k_{\mathrm{chem}} + k_{\mathrm{D}})$, where k_{D} is the Smoluchowski rate constant of the encounter pair (Supplementary Note 2 and Supplementary Table 6), so that no total rate constant exceeds the diffusion limit. The computed totals reproduce the measured rate constants of 4NP and 4NP$^-$ (Supplementary Note 2).

UV–visible spectroscopy

Each nitrophenol was dissolved in deionized water to form a nitrophenol–water binary system for pH and spectrophotometric analysis. Stock solutions of each nitrophenol species were prepared at a concentration of 250 μM. All stock solutions were diluted to 50 μM to ensure the absorbance maximum was below 1 a.u. (within the linear dynamic range). The pH values of all solutions were adjusted by HCl (0.05 M)/NaOH (0.01 M) and measured using a single-junction pH electrode (Vernier pH sensor). The pH measurements were done in triplicate within the first 10 minutes of solution preparation. UV–Vis measurements were conducted using the Cary 5000 UV–Vis–NIR spectrophotometer (spectral range 200–800 nm) in quartz cuvettes (THORLABS 3500 μL fluorescence cuvette). The measurements were performed within 2 h of preparing the solutions under dark conditions at room temperature. The pure-component spectra were prepared at pH values for which the target species was strongly predominant (Supplementary Fig. 19). These conditions were identified from the pK_{a} values in Supplementary Fig. 19. Spectra were corrected for the step at the 350 nm source changeover of the spectrophotometer by offsetting the long-wavelength segment and were smoothed with a Savitzky–Golay filter (9 nm window, third order).

Absorption spectrum calculations by TD-DFT

UV–visible (UV–Vis) spectra were calculated using the Gaussian 16 software package [53]. The geometry optimization of all BrC molecules was performed at the same level. Time-dependent density functional theory (TD-DFT) was used to predict the UV–Vis spectra. As shown in Supplementary Tables 3 and 4, five functionals—PBE (PBEPBE), PBE0 (PBE1PBE), B3LYP, M06-2X, and CAM-B3LYP—were selected to calculate the excited states to predict absorption wavelengths based on the optimized structures of six selected nitrophenols at different levels. Different basis sets—6-311++G(d,p), 6-311++G(3df,2p), cc-pVDZ, aug-cc-pVDZ, and aug-cc-pVTZ—were considered. The calculations were performed using the integral equation form polarizable continuum model (IEFPCM) implicit solvation model with water as the solvent [58]. For 4NC, λ_{max} calculated with B3LYP/6-311++G(d,p) (235.6, 308.3, and 357.6 nm) compared better with experimental data (238, 309, and 345 nm) [59] than those from other methods. For $4NC^-$, PBEPBE/6-311++G(d,p) has the best performance (λ_{max} calculated values: 224.0, 285.1, 365.7, and 428.1 nm; λ_{max} experimental values [59]: 261, 333, and 426 nm). Thus, based on the computational accuracy, we selected B3LYP/6-311++G(d,p) to predict the UV–Vis spectra for neutral species and PBEPBE/6-311++G(d,p) for deprotonated species. Previous studies [60, 61] have compared UV–Vis spectra of neutral and deprotonated species using two electronic-structure methods and basis sets.

Complex refractive index calculations

The wavelength-dependent complex RI of the aqueous particle phase was calculated using a molecular polarizability model combined with a Clausius–Mossotti effective-medium treatment [62]. Following the Lorentz oscillator form of Auguié and Le Ru [63], the microscopic polarizability of the solute was written as a sum over multiple electronic oscillators,

$$\alpha_{\text{micro}}(\lambda) = \alpha_\infty + \sum_j \frac{\alpha_j \lambda_j}{\mu_j} \left[\frac{1}{1 - \lambda_j^2/\lambda^2 - i\lambda_j^2/(\lambda\mu_j)} - 1 \right] \tag{1}$$

where λ is the vacuum wavelength, α_∞ is the static polarizability, and α_j, λ_j , and μ_j are the strength parameter, resonance wavelength, and broadening parameter of oscillator j, respectively. The values of α_∞ for BrC and its aging products were obtained from DFT calculations at PBE0/def2-TZVP/PCM level (Supplementary Table 5), and the oscillator parameters were determined by fitting the imaginary part of the molecular polarizability, Im[$\alpha(\lambda)$].

The target function, $\mathrm{Im}[\alpha(\lambda)]$, was then obtained from the absorption cross section using [62]

$$\mathrm{Im}[\alpha(\lambda)] = \left[\frac{3}{(n_{\mathrm{m}}^2 + 2)}\right]^2 \frac{\lambda \varepsilon_0 n_{\mathrm{m}}}{2\pi} \sigma_{\mathrm{abs}} \tag{2}$$

where ε_0 is the vacuum permittivity and n_{m} is the wavelength-dependent refractive index of the medium (which is pure water here, obtained from Daimon and Masumura [64] at 24°C). The calculated molar absorptivity spectrum, $\varepsilon(\lambda)$ $\left(\mathrm{L\ mol^{-1}\ cm^{-1}}\right)$, was converted into the absorption cross section per molecule, σ_{abs} $(\mathrm{m^2})$; this conversion is given in Supplementary Note 3. The oscillator parameters α_j, λ_j, and μ_j (Supplementary Table 5) were then obtained by globally fitting the model $\mathrm{Im}[\alpha_{\mathrm{micro}}(\lambda)]$ to the target $\mathrm{Im}[\alpha(\lambda)]$ under bounded constraints, with initial λ_j and μ_j taken from the detected peak positions and widths. The complex refractive index $m(\lambda) = n(\lambda) + ik(\lambda)$ of the aqueous solution was then obtained from the fitted microscopic polarizability using a Clausius–Mossotti effective-medium treatment; the effective-medium relation and the extraction of $n(\lambda)$ and $k(\lambda)$ from the complex dielectric function $\varepsilon_{\mathrm{eff}}(\lambda) = \varepsilon_1(\lambda) + i\varepsilon_2(\lambda)$ are given in Supplementary Note 3.

Shortwave radiative forcing calculations

Shortwave (SW) direct radiative forcing was calculated from the wavelength-dependent complex refractive indices of 4NP and its transformation products using the libRadtran radiative transfer package (version 2.0.6) [65, 66] with DISORT [67]. For each compound, Mie calculations were first performed to obtain the spectral extinction efficiency, single-scattering albedo, and asymmetry parameter from the calculated complex refractive index, assuming a lognormal size distribution with $r_{\mathrm{eff}} = 0.15$ µm and $\sigma_g = 1.5$. This choice was intended to represent fine/accumulation-mode nitrated-phenol aerosol, consistent with field measurements showing that nitroaromatic compounds are distributed predominantly in submicron particles, with concentration maxima commonly observed at aerodynamic diameters of roughly 0.3–0.6 µm and, in some cases, extending over a broader accumulation-mode range [68, 69]. The resulting optical properties were then used as input to monochromatic radiative transfer calculations over the 300–3000 nm range, and the forcing was spectrally integrated to obtain broadband SW forcing.

Calculations were carried out for both protonated (low pH) and deprotonated (high pH) forms, and for two aerosol altitude ranges representing fresh (0–2 km) and lofted (2–5 km) smoke. The aerosol burden was fixed at 1 Tg and distributed uniformly over the Earth's surface, and the forcing was averaged over the sunlit hemisphere with the area weighting of a uniformly

covered sphere and halved for the unlit hemisphere, so the results are global-mean, mass-normalized forcing efficiencies (W m^{-2} Tg^{-1}). All calculations used DISORT with 16 streams, the US Standard Atmosphere 1976, the Kurucz solar spectrum, a Lambertian surface albedo of 0.15, and an Independent Column Approximation to account for partial cloud cover. Additional details, including the wavelength grid, solar-zenith-angle averaging, cloud treatment, and forcing definitions at the top of the atmosphere, surface, and within the atmosphere, are provided in Supplementary Note 4.

Data availability

All study data are included in the article and/or Supplementary Information.

Code availability

The code implementing the kinetic–optical box model of Supplementary Note 5, together with the input spectra and rate constants required to reproduce Supplementary Figs. 21–23 and Supplementary Table 9, has been deposited in Zenodo (DOI: 10.5281/zenodo.23226801).

Acknowledgements

This work was financially supported by the Simons Foundation (SFI-MPS-SRM-00005211). ChatGPT was used solely to assist with language polishing. All scientific content, analyses, interpretations, and conclusions were reviewed and verified by the authors.

Author contributions

Y.H. and T.C.P. designed research; Y.H., Q.L., and T.C.P. performed research; A.L. contributed analytic tools; Y.H. and T.C.P. analyzed data; and Y.H. and T.C.P. wrote the paper.

Competing interests

The authors declare no competing interest.

References

[1] Kolden, C. A., Abatzoglou, J. T., Jones, M. W. & Jain, P. Wildfires in 2024. *Nat. Rev. Earth Environ.* **6**, 237–239 (2025).

[2] Haas, O., Prentice, I. C. & Harrison, S. P. Wildfires on a changing planet. *Nat. Commun.* **17**, 1599 (2026).

[3] Jones, M. W. *et al.* Wildfires in 2025. *Nat. Rev. Earth Environ.* **7**, 334–336 (2026).

[4] Andreae, M. O. & Gelencsér, A. Black carbon or brown carbon? The nature of light-absorbing carbonaceous aerosols. *Atmos. Chem. Phys.* **6**, 3131–3148 (2006).

[5] Wang, X. *et al.* Deriving brown carbon from multiwavelength absorption measurements: method and application to AERONET and Aethalometer observations. *Atmos. Chem. Phys.* **16**, 12733–12752 (2016).

[6] Zhang, A. *et al.* Modeling the global radiative effect of brown carbon: a potentially larger heating source in the tropical free troposphere than black carbon. *Atmos. Chem. Phys.* **20**, 1901–1920 (2020).

[7] Chakrabarty, R. K. *et al.* Shortwave absorption by wildfire smoke dominated by dark brown carbon. *Nat. Geosci.* **16**, 683–688 (2023).

[8] Fang, W. *et al.* Combined influences of sources and atmospheric bleaching on light absorption of water-soluble brown carbon aerosols. *npj Clim. Atmos. Sci.* **6**, 104 (2023).

[9] Qiu, Y. *et al.* Observational evidence of brown carbon photobleaching in urban atmosphere at molecular level. *Environ. Sci. Technol. Lett.* **11**, 1032–1039 (2024).

[10] Duan, J. *et al.* Aromatic nitration enhances absorption of biomass burning brown carbon in an oxidizing urban environment. *Environ. Sci. Technol.* **58**, 17344–17354 (2024).

[11] Witkowski, B., Jain, P. & Gierczak, T. Aqueous chemical bleaching of 4-nitrophenol brown carbon by hydroxyl radicals; products, mechanism, and light absorption. *Atmos. Chem. Phys.* **22**, 5651–5663 (2022).

[12] Kitanovski, Z., Shahpoury, P., Samara, C., Voliotis, A. & Lammel, G. Composition and mass size distribution of nitrated and oxygenated aromatic compounds in ambient particulate matter from southern and central Europe – implications for the origin. *Atmos. Chem. Phys.* **20**, 2471–2487 (2020).

[13] Yuan, W. *et al.* Measurement report: PM2.5-bound nitrated aromatic compounds in Xi'an, Northwest China – seasonal variations and contributions to optical properties of brown carbon. *Atmos. Chem. Phys.* **21**, 3685–3697 (2021).

[14] Yang, Z., Tsona, N. T., George, C. & Du, L. Nitrogen-containing compounds enhance light absorption of aromatic-derived brown carbon. *Environ. Sci. Technol.* **56**, 4005–4016 (2022).

[15] Cao, M., Yu, W., Chen, M. & Chen, M. Characterization of nitrated aromatic compounds in fine particles from Nanjing, China: Optical properties, source allocation, and secondary processes. *Environ. Pollut.* **316**, 120650 (2023).

[16] Harrison, M. A. J. *et al.* Nitrated phenols in the atmosphere: a review. *Atmos. Environ.* **39**, 231–248 (2005).

[17] Yang, W. *et al.* Important yet overlooked HONO source from aqueous-phase photochemical oxidation of nitrophenols. *Environ. Sci. Technol.* **58**, 15722–15731 (2024).

[18] Pye, H. O. T. *et al.* The acidity of atmospheric particles and clouds. *Atmos. Chem. Phys.* **20**, 4809–4888 (2020).

[19] Phillips, S. M., Bellcross, A. D. & Smith, G. D. Light absorption by brown carbon in the southeastern United States is pH-dependent. *Environ. Sci. Technol.* **51**, 6782–6790 (2017).

[20] Hennigan, C. J. *et al.* pH dependence of brown-carbon optical properties in cloud water. *Atmos. Chem. Phys.* **23**, 14437–14449 (2023).

[21] Zhao, R. *et al.* Photochemical processing of aqueous atmospheric brown carbon. *Atmos. Chem. Phys.* **15**, 6087–6100 (2015).

[22] Knight, J. W. *et al.* Wavelength- and pH-dependent optical properties of aqueous aerosol particles containing 4-nitrocatechol. *ACS Earth Space Chem.* **8**, 2198–2208 (2024).

[23] Liu, Y. & Daum, P. H. Relationship of refractive index to mass density and self-consistency of mixing rules for multicomponent mixtures like ambient aerosols. *J. Aerosol Sci.* **39**, 974–986 (2008).

[24] Navarro-Barboza, H. *et al.* Characterization of brown carbon absorption in different European environments through source contribution analysis. *Atmos. Chem. Phys.* **25**, 2667–2694 (2025).

[25] Zhou, J. *et al.* Source-explicit estimation of brown carbon in the polluted atmosphere over the North China Plain: implications for distribution, absorption, and the direct radiative effect. *Atmos. Chem. Phys.* **25**, 7563–7580 (2025).

[26] Guo, Y. *et al.* Improving low-cost optical PM sensor accuracy in humid conditions via aerosol liquid water estimation using U.S. EPA CSN data. *ACS ES&T Air* **3**, 326–335 (2026).

[27] Yang, H. *et al.* Molecular dynamics-guided reaction discovery reveals endoperoxide-to-alkoxy radical isomerization as key branching point in α-pinene ozonolysis. *Nat. Commun.* **16**, 661 (2025).

[28] Laskin, A., West, C. P. & Hettiyadura, A. P. S. Molecular insights into the composition, sources, and aging of atmospheric brown carbon. *Chem. Soc. Rev.* **54**, 1583–1612 (2025).

[29] Zhao, L., Ma, J. & Sun, Z.-z. Oxidation products and pathway of ceramic honeycomb-catalyzed ozonation for the degradation of nitrobenzene in aqueous solution. *Appl. Catal., B* **79**, 244–253 (2008).

[30] Sun, Y. L., Zhang, Q., Anastasio, C. & Sun, J. Insights into secondary organic aerosol formed via aqueous-phase reactions of phenolic compounds based on high resolution mass spectrometry. *Atmos. Chem. Phys.* **10**, 4809–4822 (2010).

[31] Hems, R. F. & Abbatt, J. P. D. Aqueous phase photo-oxidation of brown carbon nitrophenols: Reaction kinetics, mechanism, and evolution of light absorption. *ACS Earth Space Chem.* **2**, 225–234 (2018).

[32] Huo, Y. *et al.* Effect of pH on UV/H2O2-mediated removal of single, mixed and halogenated parabens from water. *J. Hazard. Mater.* **462**, 132818 (2024).

[33] García Einschlag, F. S., Carlos, L. & Capparelli, A. L. Competition kinetics using the UV/H_2O_2 process: A structure reactivity correlation for the rate constants of hydroxyl radicals toward nitroaromatic compounds. *Chemosphere* **53**, 1–7 (2003).

[34] Biswal, J., Paul, J., Naik, D. B., Sarkar, S. K. & Sabharwal, S. Radiolytic degradation of 4-nitrophenol in aqueous solutions: Pulse and steady state radiolysis study. *Radiat. Phys. Chem.* **85**, 161–166 (2013).

[35] Serpone, N. *et al.* Sonochemical oxidation of phenol and three of its intermediate products in aqueous media: Catechol, hydroquinone, and benzoquinone. Kinetic and mechanistic aspects. *Res. Chem. Intermed.* **18**, 183–202 (1993).

[36] Li, F. *et al.* Aqueous-phase chemistry of atmospheric phenolic compounds: A critical review of laboratory studies. *Sci. Total Environ.* **856**, 158895 (2023).

[37] Huo, Y. *et al.* Rapid oxidation of phenolic compounds by O3 and HO·: effects of the air–water interface and mineral dust in tropospheric chemical processes. *Atmos. Chem. Phys.* **24**, 12409–12423 (2024).

[38] Fan, X. *et al.* The aging behaviors of chromophoric biomass burning brown carbon during dark aqueous hydroxyl radical oxidation processes in laboratory studies. *Atmos. Environ.* **205**, 9–18 (2019).

[39] Mo, Y. *et al.* The influence of solvent and pH on determination of the light absorption properties of water-soluble brown carbon. *Atmos. Environ.* **161**, 90–98 (2017).

[40] Tsutsuki, K. & Kuwatsuka, S. Chemical studies on soil humic acids: VII. pH-dependent nature of the ultraviolet and visible absorption spectra of humic acids. *Soil Sci. Plant Nutr.* **25**, 373–384 (1979).

[41] Baes, A. U. & Bloom, P. R. Fulvic acid ultraviolet-visible spectra: Influence of solvent and pH. *Soil Sci. Soc. Am. J.* **54**, 1248–1254 (1990).

[42] Hinrichs, R. Z., Buczek, P. & Trivedi, J. J. Solar absorption by aerosol-bound nitrophenols compared to aqueous and gaseous nitrophenols. *Environ. Sci. Technol.* **50**, 5661–5667 (2016).

[43] Jones, S. H., Friederich, P. & Donaldson, D. J. Photochemical aging of levitated aqueous brown carbon droplets. *ACS Earth Space Chem.* **5**, 749–754 (2021).

[44] Saleh, R., Cheng, Z. & Atwi, K. The brown–black continuum of light-absorbing combustion aerosols. *Environ. Sci. Technol. Lett.* **5**, 508–513 (2018).

[45] Teich, M. *et al.* Contributions of nitrated aromatic compounds to the light absorption of water-soluble and particulate brown carbon in different atmospheric environments in Germany and China. *Atmos. Chem. Phys.* **17**, 1653–1672 (2017).

[46] Thapliyal, P., Soni, A. & Gupta, T. Field validation of brown carbon absorption dependence on acidity and aerosol liquid water content. *Atmos. Res.* **315**, 107868 (2025).

[47] Chylek, P. *et al.* Mie scattering captures observed optical properties of ambient biomass burning plumes assuming uniform black, brown, and organic carbon mixtures. *J. Geophys. Res. Atmos.* **124**, 11406–11427 (2019).

[48] Zhai, J. *et al.* Source-dependent optical properties and molecular characteristics of atmospheric brown carbon. *Atmos. Chem. Phys.* **25**, 7959–7972 (2025).

[49] Haywood, J. M. & Ramaswamy, V. Global sensitivity studies of the direct radiative forcing due to anthropogenic sulfate and black carbon aerosols. *J. Geophys. Res. Atmos.* **103**, 6043–6058 (1998).

[50] Choi, M. & Ying, Q. Modeling the impacts of open biomass burning on regional O3 and PM2.5 in Southeast Asia considering light absorption and photochemical bleaching of brown carbon. *Atmos. Environ.* **342**, 120942 (2025).

[51] Liu, X. *et al.* Secondary formation of atmospheric brown carbon in China haze: Implication for an enhancing role of ammonia. *Environ. Sci. Technol.* **57**, 11163–11172 (2023).

[52] ChemAxon. Chemicalize. https://chemicalize.com/ (2025). Property predictions performed in June 2025; developed by ChemAxon.

[53] Frisch, M. J. *et al.* *Gaussian 16* (Gaussian, Inc., Wallingford CT, 2016).

[54] Zhang, Y., Liu, J., Ghoshal, S. & Moores, A. Density functional theory calculations decipher complex reaction pathways of 6:2 fluorotelomer sulfonate to perfluoroalkyl carboxylates initiated by hydroxyl radical. *Environ. Sci. Technol.* **55**, 16655–16664 (2021).

[55] Barrios, B., Mohrhardt, B., Doskey, P. V. & Minakata, D. Mechanistic insight into the reactivities of aqueous-phase singlet oxygen with organic compounds. *Environ. Sci. Technol.* **55**, 8054–8067 (2021).

[56] Okuno, Y. Theoretical investigation of the mechanism of the Baeyer–Villiger reaction in nonpolar solvents. *Chem. Eur. J.* **3**, 212–218 (1997).

[57] Galano, A. & Alvarez-Idaboy, J. R. A computational methodology for accurate predictions of rate constants in solution: Application to the assessment of primary antioxidant activity. *J. Comput. Chem.* **34**, 2430–2445 (2013).

[58] Miertuš, S., Scrocco, E. & Tomasi, J. Electrostatic interaction of a solute with a continuum. A direct utilizaion of AB initio molecular potentials for the prevision of solvent effects. *Chem. Phys.* **55**, 117–129 (1981).

[59] Cornard, J.-P., Rasmiwetti & Merlin, J.-C. Molecular structure and spectroscopic properties of 4-nitrocatechol at different pH: UV–visible, Raman, DFT and TD-DFT calculations. *Chem. Phys.* **309**, 239–249 (2005).

[60] Grabarek, D. & Andruniów, T. Assessment of functionals for TDDFT calculations of one- and two-photon absorption properties of neutral and anionic fluorescent proteins chromophores. *J. Chem. Theory Comput.* **15**, 490–508 (2019).

[61] Singh, B. G. & Upadhyaya, H. P. Experimental and theoretical studies on reaction kinetics, mechanism, and degradation of quinoline-based herbicide with hydroxyl radical, sulphate radical anion, and hydrated electron. *ChemPhysChem* **26**, e202401135 (2025).

[62] Djorovic, A., Meyer, M., Darby, B. L. & Le Ru, E. C. Accurate modeling of the polarizability of dyes for electromagnetic calculations. *ACS Omega* **2**, 1804–1811 (2017).

[63] Auguié, B. & Le Ru, E. C. Optical absorption of dye molecules in a spherical shell geometry. *J. Phys. Chem. C* **122**, 19110–19115 (2018).

[64] Daimon, M. & Masumura, A. Measurement of the refractive index of distilled water from the near-infrared region to the ultraviolet region. *Appl. Opt.* **46**, 3811–3820 (2007).

[65] Mayer, B. & Kylling, A. Technical note: The libRadtran software package for radiative transfer calculations – description and examples of use. *Atmos. Chem. Phys.* **5**, 1855–1877 (2005).

[66] Emde, C. *et al.* The libRadtran software package for radiative transfer calculations (version 2.0.1). *Geosci. Model Dev.* **9**, 1647–1672 (2016).

[67] Stamnes, K., Tsay, S.-C., Wiscombe, W. & Jayaweera, K. Numerically stable algorithm for discrete-ordinate-method radiative transfer in multiple scattering and emitting layered media. *Appl. Opt.* **27**, 2502–2509 (1988).

[68] Liang, Y. *et al.* Size distributions of nitrated phenols in winter at a coastal site in north China and the impacts from primary sources and secondary formation. *Chemosphere* **250**, 126256 (2020).

[69] Frka, S. *et al.* Seasonal variability of nitroaromatic compounds in ambient aerosols: Mass size distribution, possible sources and contribution to water-soluble brown carbon light absorption. *Chemosphere* **299**, 134381 (2022).

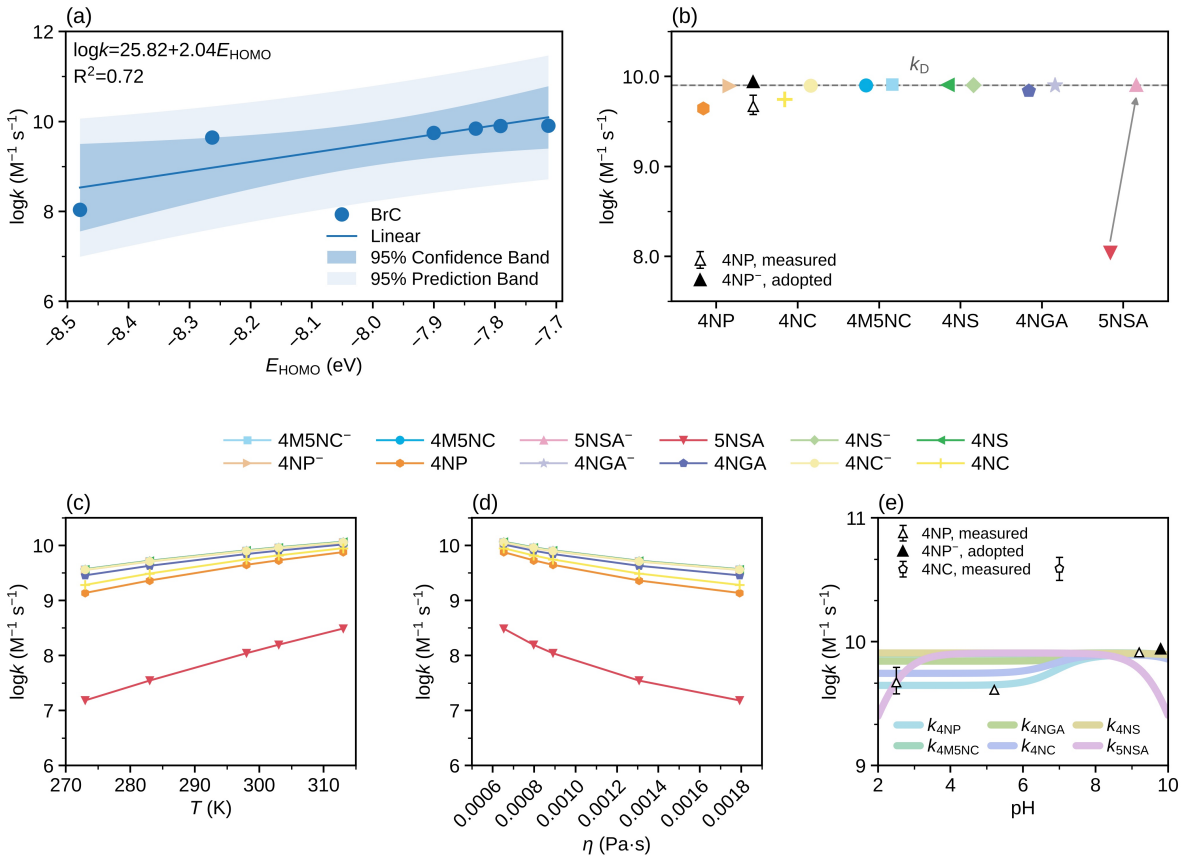

Fig. 1 Computed rate constants for the reaction of BrC with ·OH at the 1 M standard state. **a** log k of the neutral species at 298 K against E_{HOMO}, with a linear fit and its 95% confidence and prediction bands. **b** log k of the neutral (dark symbols) and deprotonated (light symbols) form of each compound at 298 K; arrows mark the change on deprotonation, and the dashed line marks k_D, (7.8–8.1) × 10^9 M^{-1} s^{-1} (Supplementary Table 6). **c** Temperature, **d** viscosity and **e** pH dependence of k (Supplementary Note 2 and Supplementary Tables 7 and 8). The plateaus in **e** above the phenolic pK_a lie at k_D; $5NSA^{2-}$ is not computed and is given $k = 0$, so the 5NSA curve falls above pH 9. Black symbols in **b** and **e** are measured rate constants for 4NP, (3.8–6.2) × 10^9 M^{-1} s^{-1} at pH < 3, 4.1 × 10^9 M^{-1} s^{-1} at pH 5.2 and twice that value at pH 9.2, and 8.7 × 10^9 M^{-1} s^{-1} for the anion [11, 33, 34], and in **e** for 4NC at pH 7 [17].

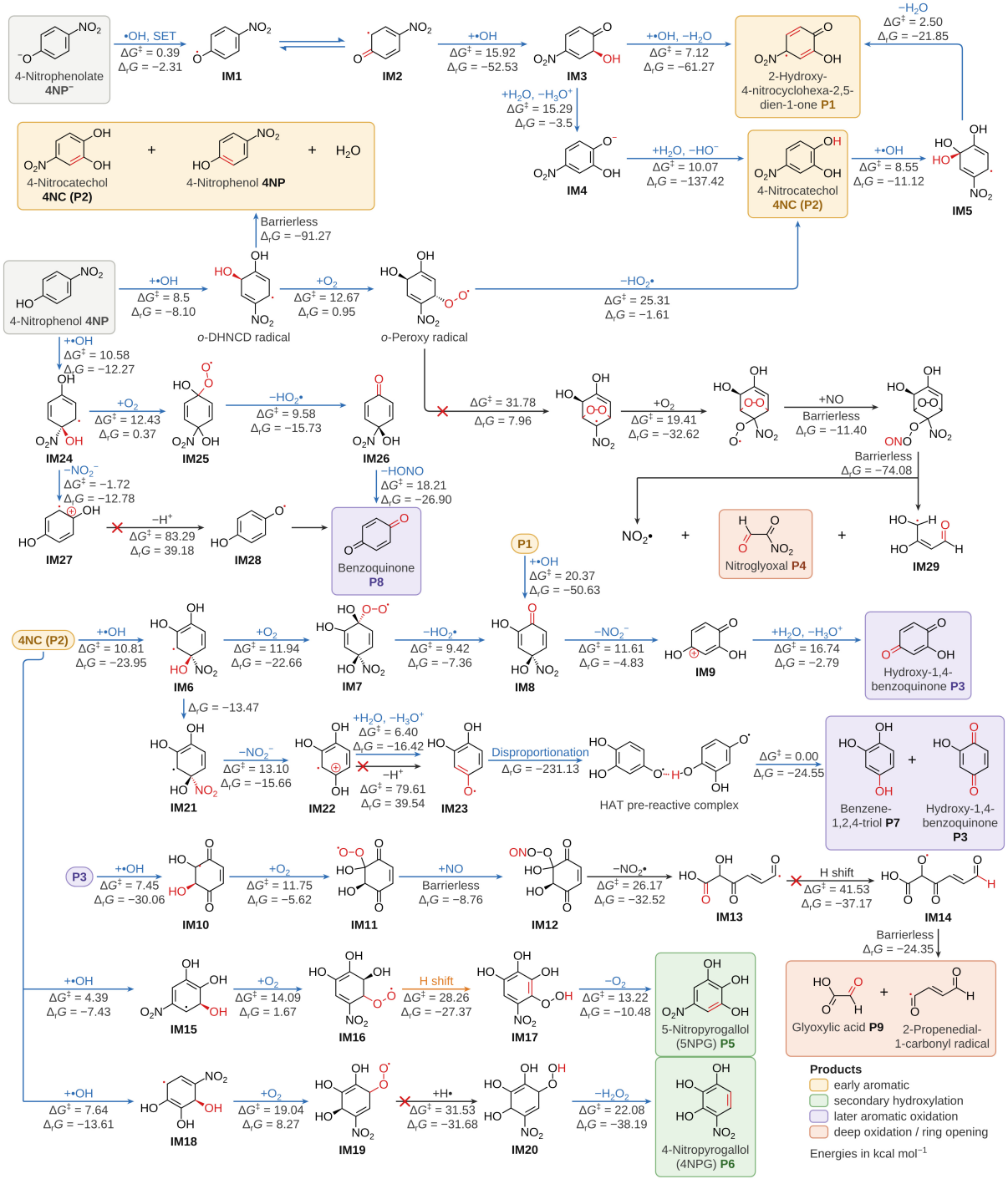

Fig. 2 Proposed subsequent aqueous-phase aging pathways following initial ·OH attack on 4NP/4NC. The products are grouped into early aromatic products (P1 and P2/4NC), secondary hydroxylation products (P5 and P6), later aromatic oxidation products (P3, P7 and P8) and deep-oxidation/ring-opening products (P4 and P9). $\Delta G^{\ddagger}$ and $\Delta_r G$ are in kcal mol^{-1}; red crosses mark kinetically unfavorable steps. Names of the intermediates are given in Supplementary Table 10.

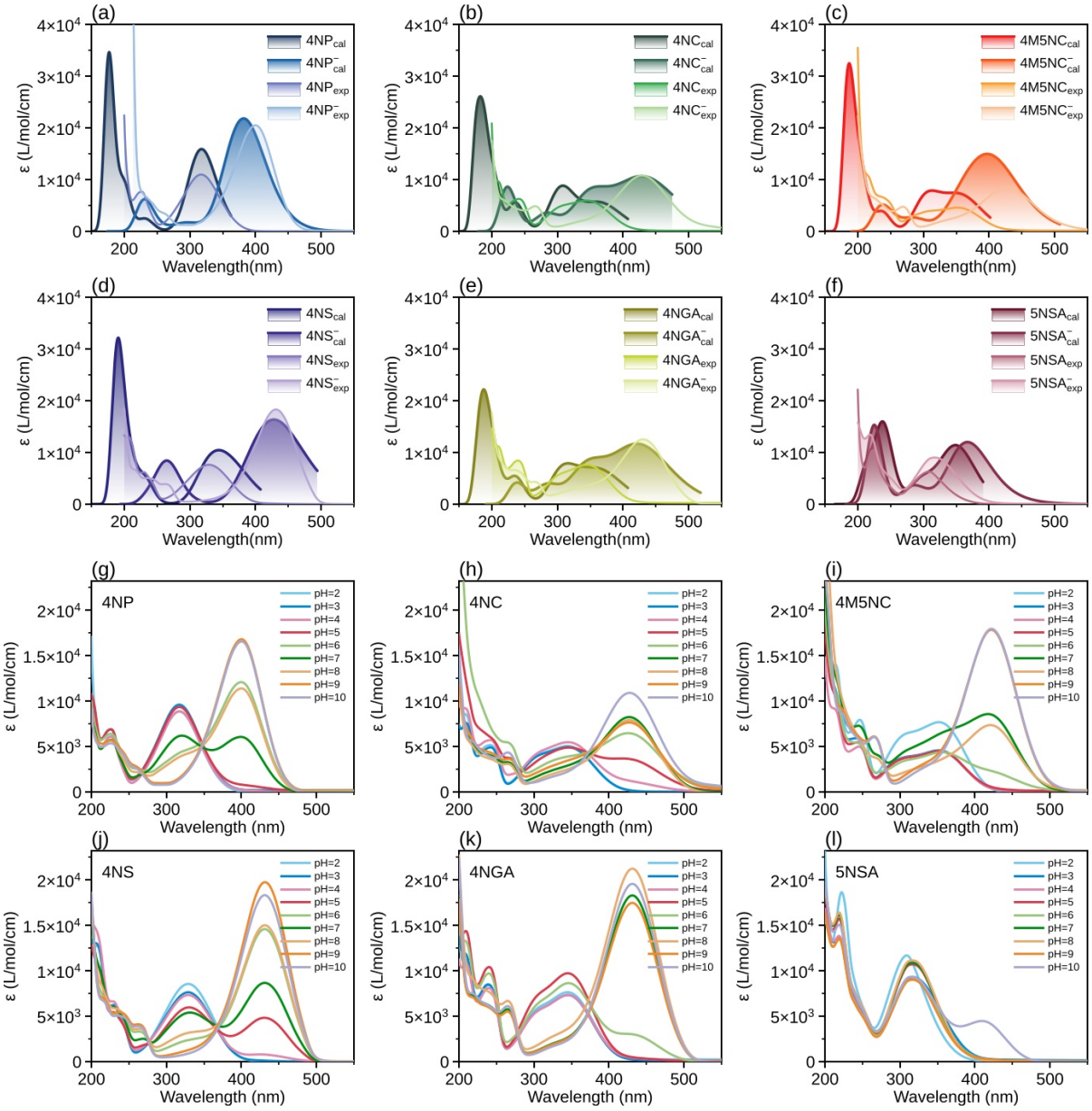

Fig. 3 Comparisons **a–f** of experimental and calculated UV–Vis spectra and **g–l** of experimental spectra measured at pH 2–10 for neutral and deprotonated BrC.

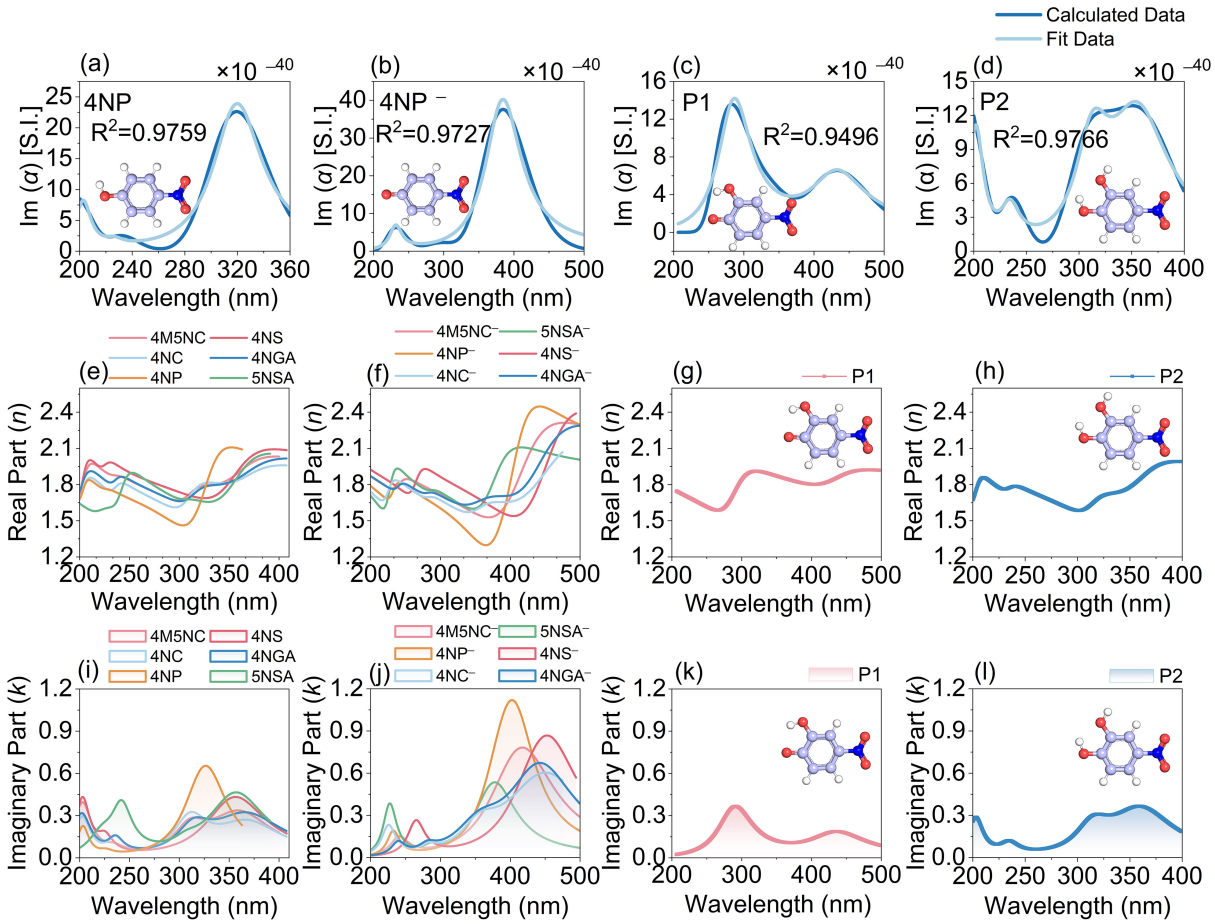

Fig. 4 **a**–**d** Fitting of the imaginary part of the molecular polarizability of the neutral and deprotonated forms of 4NP and their transformation products; **e**–**h** the real part of the complex RI of the neutral and deprotonated forms of BrC, P1, and P2; and **i**–**l** the imaginary part of the complex RI of the neutral and deprotonated forms of BrC, P1, and P2. Atom colors are as follows: red for O, light purple for C, white for H, and dark blue for N.

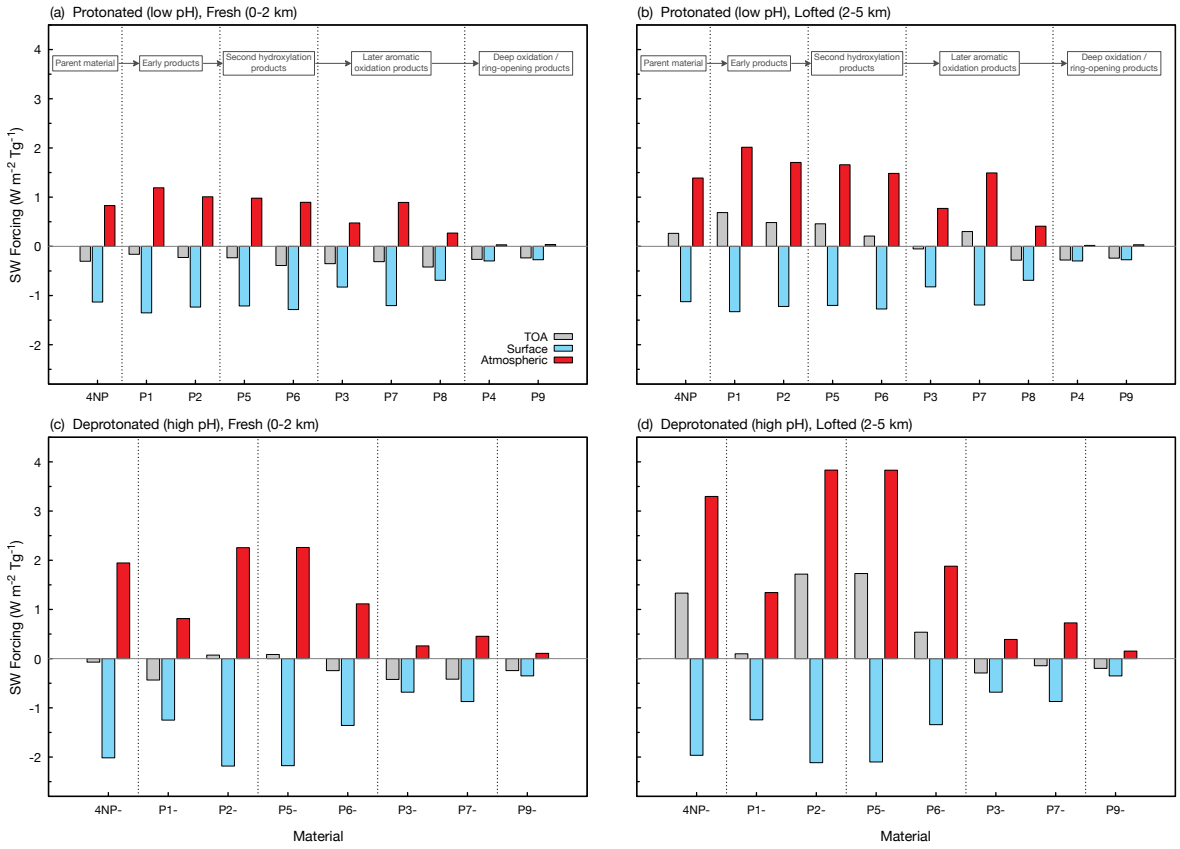

Fig. 5 All-sky shortwave (SW) radiative forcing decomposition for 4NP and its aging products under low pH and high pH conditions for fresh (0–2 km) and lofted (2–5 km) smoke layers. Gray, blue, and red bars denote shortwave forcing at the top of the atmosphere (TOA), surface, and within the atmosphere, respectively, normalized by aerosol burden (W m^{-2} Tg^{-1}) and averaged over the globe for a cloud fraction of 0.6 with the cloud between 1.5 and 2.5 km. Materials are arranged by aging stage from parent material to deep-oxidation/ring-opening products. More strongly absorbing aromatic products and their deprotonated analogues show larger positive atmospheric forcing and more negative surface forcing than the ring-opening products. P4 and P8 have no deprotonated form in the modeled set (Supplementary Table 11) and are therefore absent from **c** and **d**.